CMS Physics Analysis Summary

Search for Higgs boson pair production in the final state containing two photons and two bottom quarks in proton-proton collisions at $\sqrt{s} = 13$ TeV

The CMS Collaboration

Abstract

A search is presented for the production of a pair of Higgs bosons, where one decays into two photons and the other to two bottom quarks. Both resonant and nonresonant production mechanisms of the Higgs boson pair are investigated. The analysis is performed using proton-proton collision data from the LHC at $\sqrt{s} = 13$ TeV recorded by the CMS detector in 2016, which corresponds to an integrated luminosity of 35.9 fb^{-1}. The observed data are in agreement with standard model predictions. Upper limits on the production cross sections of spin-0 and spin-2 particles are set at 95% confidence level, excluding a product of the production cross section and branching fraction of narrow-width particles between 0.26 and 3.67 fb for spin-0 and between 0.21 and 3.61 fb for spin-2. In addition, an upper limit on the cross section for nonresonant Higgs boson pair production is set and compared to standard model Higgs boson pair production via gluon fusion. Constraints on anomalous couplings that affect Higgs boson pair production are also determined. For the standard model hypothesis, the data exclude a product of production cross section and branching fraction larger than 1.67 fb at 95% confidence level, corresponding to 19.2 times the standard model prediction.

1 Introduction

The discovery of a boson with a mass of approximately 125 GeV, with properties close to those expected for the Higgs boson (H) of the standard model (SM) [1, 2], has stimulated interest in the exploration of the Higgs potential. The production of a pair of Higgs bosons (HH) is a rare process that is sensitive to the structure of this potential through the Higgs boson's self-coupling mechanism. In the SM, the cross section for the production of two Higgs bosons in proton-proton (pp) collisions at 13 TeV is 33.49 ± 1.4 fb for the gluon-gluon fusion process [3, 4], which lies beyond the reach of analyses based on the first runs of the CERN LHC.

Many theories beyond the SM (BSM) suggest the existence of heavy particles that can couple to a pair of Higgs bosons. These particles could appear as a resonant contribution in the invariant mass of the HH system. If the new particles are too heavy to be observed through a direct search, they may contribute to the HH production through virtual processes (as shown, e.g., in Refs. [5, 6]).

Models with warped extra dimensions (WED) [7], which postulate the existence of one compactified extra spatial dimension, are among the models that predict new resonances decaying to a Higgs boson pair. WED models predict both spin-0 (radions [8–10]), and spin-2 (gravitons [11–13]) new states that can be directly detected at the LHC experiments. A specific realization of the WED models in which both the radion and graviton fields, and the SM fields can propagate in the extra dimension (bulk RS model [14]) is chosen as a benchmark scenario. Another phenomenogically well-motivated BSM model that is able to induce resonant HH enhancements is the two Higgs doublet model (2HDM) [15, 16], in which a second complex scalar doublet field is added to the SM scalar sector.

Different BSM models can also induce modifications in the Higgs boson's fundamental couplings relative to their SM values (as shown, for example, in Refs. [17–19]). Two coupling modifiers are assumed to quantify BSM deviations from couplings that exist on the SM: κ_λ, which measures deviations from the SM predicted Higgs self-coupling parameter ($\kappa_\lambda \equiv \lambda/\lambda_{SM}$), and κ_t, which measures deviations from the SM predicted top quark Yukawa coupling to the Higgs boson ($\kappa_t \equiv y_t/y_{t,SM}$). Purely BSM anomalous couplings can also be introduced in this analysis. In particular, anomalous contact interactions between two Higgs bosons and two top quarks (c_2), between one Higgs boson and two gluons (c_g), and two Higgs bosons and two gluons (c_{2g}). The HH production cross section as a function of these five parameters has been parametrized at LO [20] and approximately extended to NNLO+NNLL [3, 21, 22], and is based on the modified SM Lagrangian which relevant part is in the following equation [23]:

$$\Delta\mathcal{L} = \kappa_\lambda \, \lambda_{SM} v \, \mathrm{H}^3 - \frac{m_\mathrm{t}}{v}\left(v + \kappa_t \, \mathrm{H} + \frac{c_2}{v}\,\mathrm{H}^2\right)(\bar{\mathrm{t}}_\mathrm{L}\mathrm{t}_\mathrm{R} + h.c.) + \frac{1}{4}\frac{\alpha_s}{3\pi v}\left(c_g\,\mathrm{H} - \frac{c_{2g}}{2v}\,\mathrm{H}^2\right)G^{\mu\nu}G_{\mu\nu}\,, \quad (1)$$

where t_L and t_R are the top quark fields with left and right chiralities, respectively, H is the physical Higgs boson field, and $G^{\mu\nu}$ is the gluon field strength tensor. Five main Feynman diagrams can be constructed from the above Lagrangian (see Figure 1), each corresponding to a matrix element associated to different combinations of BSM parameters and different properties of the HH final state.

This paper describes a search for the production of pairs of Higgs bosons in the $b\bar{b}\gamma\gamma$ final state in pp collisions at the LHC, using data corresponding to an integrated luminosity of 35.9 fb^{-1} collected by the CMS experiment at $\sqrt{s} = 13$ TeV. Both nonresonant and resonant production are explored, with the search for a narrow resonance X conducted at masses m_X between
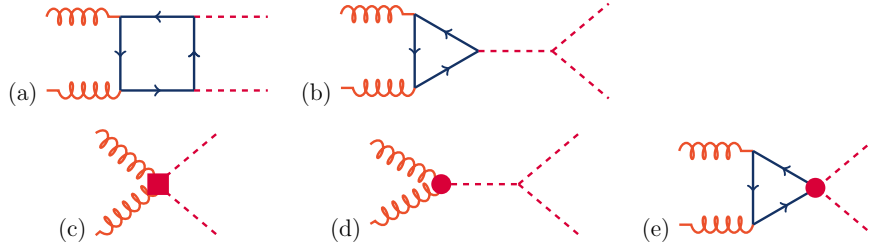
Figure 1: Feynman diagrams that contribute to HH production by gluon-gluon fusion at leading order. Diagrams (a) and (b) correspond to SM-like processes, while diagrams (c), (d), and (e) correspond to pure BSM effects: (c) and (d) describe contact interactions between the H boson and gluons, and (e) exploits the contact interaction of two H bosons with top quarks.

250 and 900 GeV. The fully-reconstructed $b\bar{b}\gamma\gamma$ final state discussed in this paper combines the large SM branching fraction ($\mathcal{B}$) of the H $\to$ b$\bar{b}$ decay with the comparatively low background and good mass resolution of the H $\to \gamma\gamma$ channel, yielding a total $\mathcal{B}(\text{HH} \to b\bar{b}\gamma\gamma)$ of 0.26% [24]. The search exploits the mass spectra of the diphoton ($M(\gamma\gamma)$), dijet ($M(jj)$), and the four-body systems ($M(jj\gamma\gamma)$), as well as the helicity angles describing the HH production and decay to provide discrimination between production of two Higgs bosons and SM background.

A search in the same final state was performed by the CMS [25] and ATLAS [26] collaborations, with data taken at $\sqrt{s} = 8$ TeV. Complementary final states such as HH $\to$ b$\bar{b}$b$\bar{b}$, HH $\to \tau\tau$b$\bar{b}$, and HH to multileptons and multiphotons were also explored by the ATLAS [27, 28] and CMS [29–32] collaborations.

This paper is organized as follows: Section 2 contains a brief description of the CMS detector. In Section 3 we describe the simulated signal and background event samples used in the analysis. Section 4 is dedicated to the discussion of event selection and Higgs boson reconstruction. The event classification and signal extraction procedures are discussed in Section 5. In Section 6 we present the systematic uncertainties impacting each analysis method. Section 7 contains the results of resonant and nonresonant searches, and Section 8 provides a summary.

2 The CMS detector

The CMS detector, its coordinate system, and main kinematic variables used in the analysis are described in detail in Ref. [33]. The detector is a multipurpose apparatus designed to study physics processes at large transverse momentum p_T in pp and heavy-ion collisions. The central feature of the apparatus is a superconducting solenoid, of 6 m internal diameter, providing a magnetic field of 3.8 T. A silicon pixel and strip tracker covering the pseudorapidity range $|\eta| < 2.5$, a crystal electromagnetic calorimeter (ECAL), and a brass and scintillator hadron calorimeter (HCAL) reside within the field volume. The ECAL is made of lead tungstate crystals, while the HCAL has layers of plates of brass and plastic scintillator. These calorimeters are both composed of a barrel and two endcap sections and provide coverage up to $|\eta| < 3.0$. An iron and quartz-fibre Cherenkov hadron calorimeter covers larger values of $3.0 < |\eta| < 5.0$. Muons are measured in the $|\eta| < 2.4$ range, using detection planes based on three technologies: drift tubes, cathode strip chambers, and resistive-plate chambers.

The first level of the CMS trigger system, composed of special hardware processors, uses information from the calorimeters and muon detectors to select the most interesting events in a

time interval of less than $4\,\mu$s. The high-level trigger (HLT) processor farm further decreases the event rate from around $100\,$kHz to less than $1\,$kHz, before data storage.

3 Simulated events

Signal samples are simulated at leading order using `MG5_aMC@NLO` interfaced with *LHAPDF6* [34, 35]. The PDF4LHC NLO PDF set is used [36]. The events are then processed with PYTHIA 8 [37] for showering and hadronization and GEANT4 [38] for a simulation of the CMS detector. The models provide a description of production through gluon-gluon fusion of particles with narrow width (width set to 1 MeV) that decay to two Higgs bosons, with mass $m_{\mathrm{H}} = 125\,$GeV, in agreement with Ref. [39]. Events are generated either for spin-0 radion production, or spin-2 KK-graviton production predicted by the bulk-RS model.

As previously mentioned, the nonresonant part of this analysis focuses both on the SM-like HH production and its modifications via anomalous couplings that are parametrized through five effective couplings (κ_λ, κ_t, c_2, c_g, and c_{2g}). To avoid a prohibitively large number of samples to simulate, a method to partition the 5 dimensional (5D) parameter space into regions with similar kinematics was designed in Refs. [40–42]. The method suggests the simulation of 12 samples with BSM values for the effective couplings which, along with the sample assuming all SM-like parameters (SM-like HH production) and the sample assuming no HH production via the Higgs self-coupling (all couplings set to 0, except $\kappa_t = 1$). These samples can be reweighted into any desired point of the full 5D parameter space utilizing the generator level information about the HH system. The 14 nonresonant signal samples have been generated with the same simulation setup as the resonant samples described previously.

The dominant background processes to the $\mathrm{b\bar{b}\gamma\gamma}$ final state are those in which two objects identified as photons (either prompt photons or jets misidentified as photons) are produced via QCD, in association with jets. These processes contribute with a smoothly falling shape to both $M(\gamma\gamma)$ and $M(jj)$ distributions. In this analysis, these contributions are modeled entirely from the data, via a parametric fit, without the use of simulations.

The SM H $\to \gamma\gamma$ boson production via gluon-gluon fusion, as well as vector boson fusion and $\mathrm{t\bar{t}}$, $\mathrm{b\bar{b}}$ and vector boson associated production are considered as sources of background in this analysis. They are generated using `MG5_aMC@NLO` and PYTHIA 8 (VH and $\mathrm{b\bar{b}H}$), or the generator POWHEG [43–45] at NLO in QCD interface with PYTHIA 8 (gluon-gluon fusion, VBF and $\mathrm{t\bar{t}H}$), and processed through GEANT4-based detector simulation. These samples are used to simulate the events in which the SM Higgs boson decaying to two photons are selected in the analysis, along with two extra jets. This background is designated in this document as the SM single Higgs background for this analysis.

4 Dataset and Event selection

Events are selected online from data using double photon triggers. These triggers require two photons with transverse energy (E_{T}) greater than $30\,$GeV and $18\,$GeV for leading and sub-leading photons. In addition, calorimeter-based isolation and shower shape requirements, as well as a diphoton invariant mass threshold, are placed on the two photons. These photons are required to be within the ECAL fiducial region, with $|\eta(\gamma)| < 2.5$ and excluding the ECAL barrel-endcap transition region $1.44 < |\eta(\gamma)| < 1.57$.

4.1   The $H \to \gamma\gamma$ candidate

In the offline selection, events are required to have at least one well identified vertex with a distance less than $24\,cm$ away from the nominal interaction point in the z-direction and $2\,cm$ away in the xy-plane. The primary vertex is identified by a multivariate analysis designed by the analysis dedicated to the measurement of the $H \to \gamma\gamma$ production [46]. Using these criteria, less than 0.1% of simulated signal events have incorrectly identified the primary vertex in simulated signal samples.

Events are further required to have at least two photon candidates passing the following criteria: leading photon $E_T > 30\,GeV$, sub-leading photon $E_T > 20\,GeV$; leading photon $E_T/M(\gamma\gamma) > 1/3$, sub-leading photon $E_T/M(\gamma\gamma) > 1/4$; $100 < M(\gamma\gamma) < 180\,GeV$.

Photons are identified using a multivariate-based technique [47] including as inputs requirements on p_T of the electromagnetic shower, its longitudinal leakage into the HCAL, its isolation from jet activity in the event, as well as a veto on the presence of a track matching the ECAL cluster.

4.2   The $H \to b\bar{b}$ candidate

Jets are reconstructed using the anti-k_T algorithm with distance parameter $R = 0.4$. Jet candidates are required to have $p_T > 25\,GeV$ and $|\eta| < 2.4$. In addition, identification criteria are applied to remove spurious jets associated with calorimeter noise [48]. Moreover jets must be separated from the two selected photon candidates by a distance $\Delta R > 0.4$. The resulting jets are combined into dijet candidates. Only dijet candidates with $70 < M(jj) < 190\,GeV$ are considered in the analysis. The jets in the dijet candidate are then ordered by p_T, as leading and subleading jets. At least one dijet candidate is necessary for an event to be selected. In cases where more than two jets have been found, the dijet constructed with the two jets with the highest b-tagging scores is selected as the analysis dijet candidate. The combined secondary vertex algorithm (b-tagging score) is used as a proxy for the probability that a jet is a result of a b-quark hadronization [49].

The energy of the jets in this analysis are regressed according to a multivariate analysis technique, similar to what has been used for the CMS SM search for $H \to b\bar{b}$ decays [50]. This procedure corrects the absolute scale of the jets and improves the overall jet energy resolution. A main difference to the $H \to b\bar{b}$ procedure is the inclusion of missing transverse energy related variables. This has been proven beneficial in final states with no neutrinos from the hard scatter, which means that all missing energy in signal events are coming from mismeasured jets or neutrinos from hadron decays. In addition a separate training has been utlized for leading and subleading jet.

A summary of the analysis baseline selection requirements is presented in Table 1. After the diphoton and dijet candidate selections, they are combined to form an HH candidate.

4.3   The two-Higgs-boson system

To improve the resolution in $M(jj\gamma\gamma)$ for the signal, the HH mass is approximated by $\tilde{M}_X$ [51]:

$$\tilde{M}_X = M(jj\gamma\gamma) - M(jj) - M(\gamma\gamma) + 250\,\text{GeV}. \tag{2}$$

$\tilde{M}_X$ mitigates the $M(jj\gamma\gamma)$ dependency on the dijet energy resolution with the assumption that the dijet originates from a Higgs candidate decay. This procedure has an effect analogous to a kinematic fit, but without the need for analysis-level measurements of quantities such as jet's

Table 1: Summary of the analysis baseline selection criteria.

Photons		Jets	
Variable	Selection	Variable	Selection
$E_{\mathrm{T}}(\gamma_1)$	$> 30\,\mathrm{GeV}$ and $> M(\gamma\gamma)/3$	p_{T} [GeV]	> 25
$E_{\mathrm{T}}(\gamma_2)$	$> 20\,\mathrm{GeV}$ and $> M(\gamma\gamma)/4$	$\Delta R(j,\gamma)$	> 0.4
$|\eta(\gamma)|$	< 2.5	$|\eta(j)|$	< 2.4
$M(\gamma\gamma)$ [GeV]	$[100,180]$	$M(jj)$ [GeV]	$[70,190]$

energy and position resolution. The improvements of the di-Higgs invariant mass reconstruction are shown on Fig. 2. The improvement in resolution is most striking at low m_{X} where the ratio $|M(\gamma\gamma) + M(jj) - 250\,\mathrm{GeV}|/M(jj\gamma\gamma)$ is the largest. It vanishes progressively at high m_{X}. For these reasons, $\tilde{M}_{\mathrm{X}}$ will also be used as a proxy for the 4-body invariant mass in the nonresonant analysis.

Figure 2: Comparison of $\tilde{M}_{\mathrm{X}}$ (red line) of $M(jj\gamma\gamma)$ with $\tilde{M}_{\mathrm{X}}$ (purple line) for different spin-2 resonance masses. All distributions are obtained after the full baseline selection (Table 1), and are normalized to unity.

With the four objects from the HH decay being reconstructed, angular correlations in the signal can provide important information to the analysis. The scattering angle, $\theta_{\mathrm{HH}}^{\mathrm{CS}}$, is defined in the Collins–Soper (CS) frame of the four-body system state [52], as the angle between the momentum of the Higgs boson decaying into two photons and the line that bisects the acute angle between the colliding protons. Since in the CS frame, the motion axes of both Higgs boson candidates are collinear, the choice of the Higgs boson decaying to photos as reference direction is arbitrary. Therefore we use the absolute value of the cosine of this angle ($|\cos\theta_{\mathrm{HH}}^{\mathrm{CS}}|$) to obviate this arbitrariness. Finally, the decay angles of each Higgs boson between the decay products in its own rest frame and the direction of motion of the boson in the CS frame are considered. Since the two photons in the Higgs decay are indistinguishable and the charge of the b quarks are not considered in this analysis, the absolute value of these angles are used: $|\cos\theta_{\mathrm{bb}}|$ and $|\cos\theta_{\gamma\gamma}|$.

4.4   Background Composition

The QCD-induced nonresonant background is the leading contributor to the analysis' background processes. This nonresonant background, with yields about three orders of magnitude larger than the sum of the SM single Higgs processes, is fully estimated parametrically in a

data-driven way. Data control regions are also used to validate the signal extraction technique and optimizing the selection criteria. The SM single Higgs production, on the other hand, is estimated through simulations, and represents an important source of background, given its resonant structure in $M(\gamma\gamma)$. Therefore, it is important to understand how it contributes to the overall observed event yields.

In Figure 3 the data are compared to expected SM single Higgs background, in the assumed production mechanisms, after the baseline selection described in Table 1. These plots show the main kinematic properties of the $b\bar{b}\gamma\gamma$ final state that are used throughout the analysis: invariant masses $M(\gamma\gamma)$, $M(jj)$, $M(jj\gamma\gamma)$, $\tilde{M}_X$ and helicity angles $|\cos\theta_{HH}^{CS}|$, $|\cos\theta_{bb}|$. As described in Section 3, the SM single Higgs production mechanisms considered in the background composition are: gluon-gluon fusion, vector boson fusion, vector boson associated production, and $t\bar{t}$ and $b\bar{b}$ associated productions. These contributions are scaled according to their theoretical cross sections [22]. The resonant signal presented in these plots have been normalized to a cross section of 500 fb, while the SM-like HH production is normalized to 5000 times its cross section times branching fraction to $b\bar{b}\gamma\gamma$.
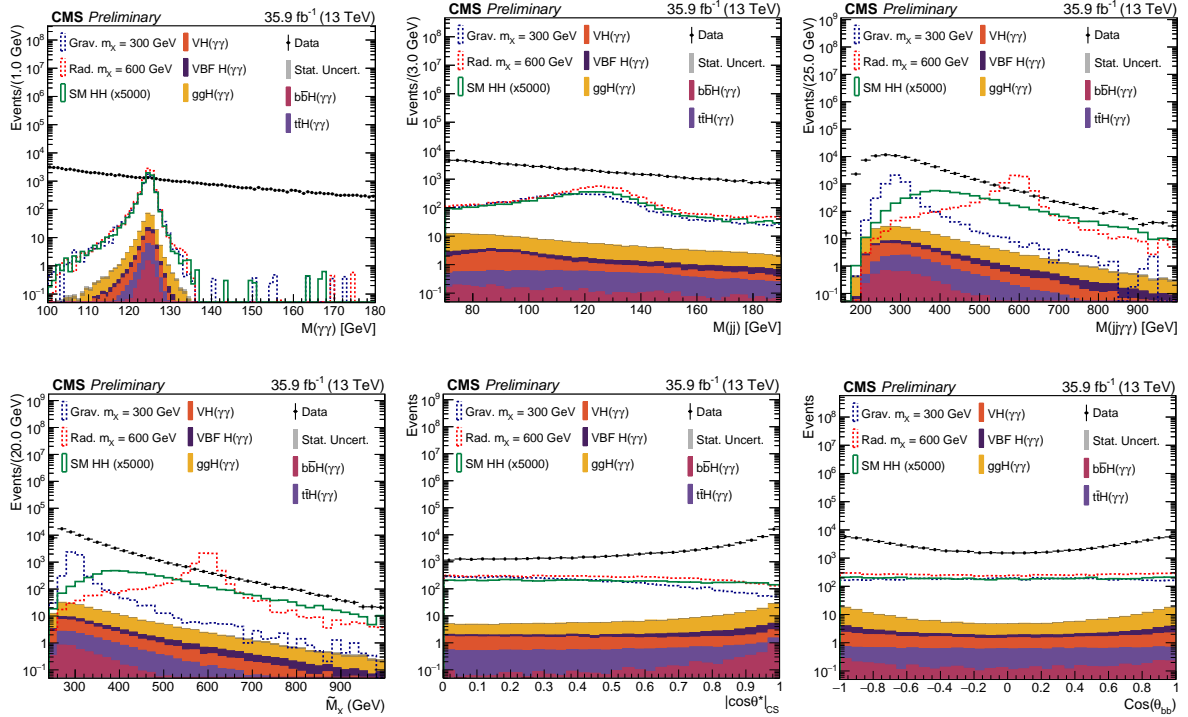

Figure 3: Data compared to the simulated background spectra after selections on photons and jets summarised in Table 1. The diphoton (pp) and prompt-fake (pf) contributions are normalized to data.

5 Analysis strategy

The analysis strategy, after dijet and diphoton candidates selection, is based on parametric fit on the two-dimensional plane defined by $M(jj)$ and $M(\gamma\gamma)$ for the signal extraction and limit setting procedure. It has been observed that this 2D signal extraction procedure helps particularly to constrain the impact of the single Higgs background in the final nonresonant result, since no resonant structure is expected in the $M(jj)$ distribution for these processes. The vector boson associated SM single Higgs production is an exception to this case, however, its contribution is not of leading importance due to its small cross section.

5.1 Event Classification

To select the most signal-like events and classify these events in categories with optimized purity contents, a multivariate analysis (MVA) is used. With this goal, a boosted decision tree (BDT) is trained with the TMVA package [53]. An important requirement to this method, in this analysis, is that the BDT output must be independent of both $M(\gamma\gamma)$ and $M(jj)$ for both signal and background. This requirement is tied to the signal extraction method used, which assumes a certain shape for these distributions. The input variables to the classification BDT training were of three types: b-tagging variables (the b-tagging score of each jet in the dijet candidate), helicity angles (as defined in Section 4.3) and HH p_T balance variables ($p_T(\gamma\gamma)/M(jj\gamma\gamma)$ and $p_T(jj)/M(jj\gamma\gamma)$). The BDT is trained with the ensemble of nonresonant signals as the signal hypothesis, in the nonresonant search, and with the ensemble of resonant signals, in the resonant search, which have been described in Section 3. This procedure mitigates the analysis sensitivity on specific signal hypotheses without compromising performance. The BDT output (classification MVA) is shown in Figure 4.
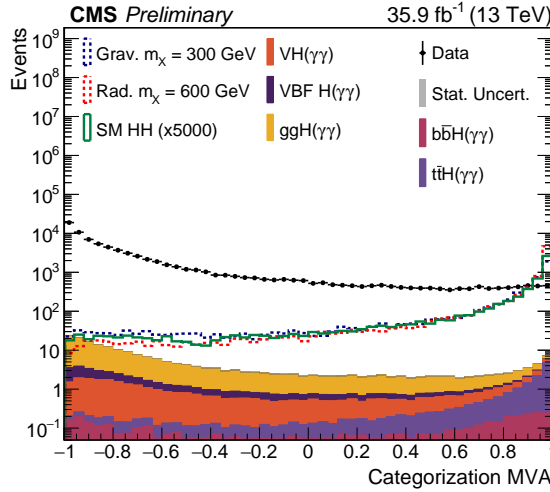

Figure 4: BDT output (classification MVA). The background and signal normalizations follow the plots presented in Section 4.4.

In the nonresonant search, an extra categorization is performed using the $\tilde{M}_X$ information. Since the SM-like nonresonant $\tilde{M}_X$ spectrum peaks at around 400 GeV, with the background distribution peaking at approximately 300 GeV, it has been found that the maximal sensitivity is achieved in the region $\tilde{M}_X > 350$ GeV. However, anomalous couplings may change the signal hypothesis $\tilde{M}_X$ distribution. Therefore, instead of imposing a $\tilde{M}_X$ selection, events are categorized, in the nonresonant search, in two regions: above (high mass region) and below the $\tilde{M}_X = 350$ GeV (low mass region). The MVA output is used, in each mass region, to define a high purity category (HPC) and a medium purity category (MPC), which are optimized by maximizing the SM-like expected cross section limit. In the nonresonant low mass, MPC region, an extra requirement is applied on the jet candidates based on a loose b-tagging criterium, in order to mitigate the impact of jets from pile-up interactions.

In the resonant search, $\tilde{M}_X$ is used primarily to constrain the signal region around the signal hypothesis mass. It has been found that slicing $\tilde{M}_X$ into mass windows covering 60% of the different resonance shapes leads to an optimal sensitivity. The exact width of this mass window is, therefore, a function of the hypothesis mass, and is constructed as the smallest $\tilde{M}_X$ interval that covers the required fraction of signal.

$\tilde{M}_X$ is also used to identify two different regions of interest in the resonant analysis. Given

its low branching fraction, but also low background yields, the $b\bar{b}\gamma\gamma$ final state is expected to be the most sensitive analysis searching for resonances decaying to HH with masses below 400 GeV, which has been verified experimentally in previous results. Therefore, the resonant analysis definition of the MVA-based categories is first optimized for this low mass region. This category definition, however, is found to be too stringent to higher resonance masses, limiting the precision of the data-driven signal extraction method used. This limiting factor is observed to begin interfering with the analysis performance for masses above $\tilde{M}_X = 600$ GeV. Another MVA-based categorization is then defined for this high mass region, allowing for higher signal and background event yields in comparison to the low mass region ($\tilde{M}_X < 600$ GeV) categorization. A summary of the categorizations performed on the resonant and nonresonant analyses are shown in Table 2.

Analysis	Region	MVA Categorization	$\tilde{M}_X$
Nonresonant	High mass	HPC: MVA > 0.97 MPC: $0.6 <$ MVA < 0.97	$\tilde{M}_X > 350\,\mathrm{GeV}$
	Low mass	HPC: MVA > 0.985 MPC: $0.6 <$ MVA < 0.985	$\tilde{M}_X < 350\,\mathrm{GeV}$
Resonant	High mass	HPC: MVA > 0.5 MPC: $0 <$ MVA < 0.5	Mass window
	Low mass	HPC: MVA > 0.96 MPC: $0.7 <$ MVA < 0.96	Mass window

Table 2: Summary of categorization strategies for the resonant and nonresonant analyses.

The typical signal efficiencies obtained in the resonant analysis are shown in Figure 5. Efficiencies for different analysis steps are shown: after the trigger selection, after the diphoton candidate selection, after the dijet candidate selection, and after the MVA categorization minimal selection. The efficiencies range from approximately 20% (low mass) to 50% (high mass) for both spin-0 and spin-2 resonance hypotheses. The efficiency for the SM-like nonresonant signal hypothesis is approximately 25% in the high mass region and 5% in the low mass region.

5.2 Signal modeling

The probability density (PD) of each invariant mass distribution used in the signal extraction procedure is modeled with a double-sided Crystal Ball (CB) function. The double-sided Crystal Ball is a version of the standard Crystal Ball function [54] which has two independent exponential tails. This modeling is useful in situations in which a lower-energy tail might be created by energy mismeasurements and a high-energy tail might be created due to by object mismatching (i.e., when a jet from pile-up interactions is selected as one of the jet candidates). The final two-dimensional signal model PD is a product of the independent $M(\gamma\gamma)$ and $M(jj)$ models. The signal modeling no-correlation hypothesis is checked by comparing the two-dimensional $M(\gamma\gamma) \times M(jj)$ distribution from the simulated signal samples and the two-dimensional PD. For the typical expected number of signal events in this analysis, the impact of such correlations is found negligible.

The PD parameters are obtained by fits to the simulated signal samples in each different analysis region. The gaussian core of the chosen PD provides a natural proxy for the energy resolu-
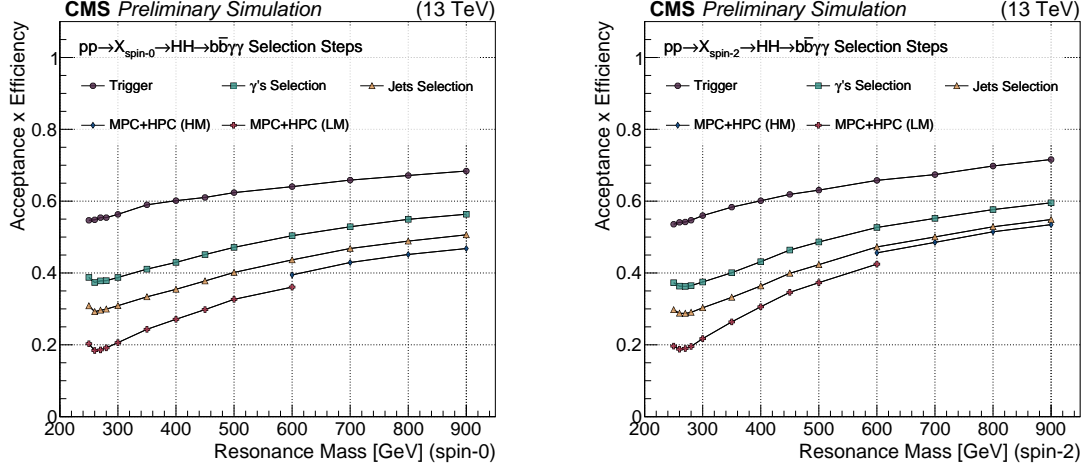
Figure 5: Acceptance times the efficiency for different resonance hypotheses: spin-0 (left) and spin-2 (right).

tion parameter. Examples of the signal shapes in the nonresonant analysis, assuming a SM-like signal, are shown in Figures 6 and 7.

5.3   Background modeling

The nonresonant background is described through polynomials in the Bernstein basis [55]. It has been observed that a second-order Bernstein polynomial fits well the observed data for regions with 15 or more fitted events. Below that, a first-order Bernstein polynomial is used. This choice of background PD was tested for possible biases in the signal extraction by comparing it to other possible background models, such as exponentials and Laurent polynomials. The bias from the chosen PD is always found to be smaller than the statistical uncertainty in the fit, and can be safely neglected [1].

The SM single Higgs background contribution is also estimated through a PD fitted to simulated SM single Higgs samples. For all the different production mechanisms, the $M(\gamma\gamma)$ distribution is modeled by a double-sided Crystal Ball. The $M(jj)$ modeling is production dependent: for gluon-fluon fusion and vector boson fusion, $M(jj)$ is modeled with a Bernstein polynomial; for the other production mechanisms, a double-sided Crystal Ball is also used. Similar to the signal modeling, the final 2D SM single Higgs model is an independent product of the $M(\gamma\gamma)$ and $M(jj)$ models.

The one-dimensional projections of the background-plus-signal fits in the nonresonant analysis' signal regions are shown in Figs. 8 and 9. In Fig. 10, the background fits are shown for the resonant analysis selection assuming a resonance with $m_X = 320$ GeV. The green dashed lines represents the nonresonant part of the expected background, modeled by a second-order Bernstein polynomial. The full background modeling PD (full red line) is the sum of this nonresonant background and the sum all SM single Higgs contributions (scaled to their cross sections). The full blue line represents the SM-like HH production, normalized to its SM cross section times a scaling factor specified in the legends. A 2D Kolmogorov-Smirnov (KS) test is performed comparing the background hypothesis with data to check for bad modeling. All fits pass the KS test prerequisite of having the KS probability larger than 0.05.
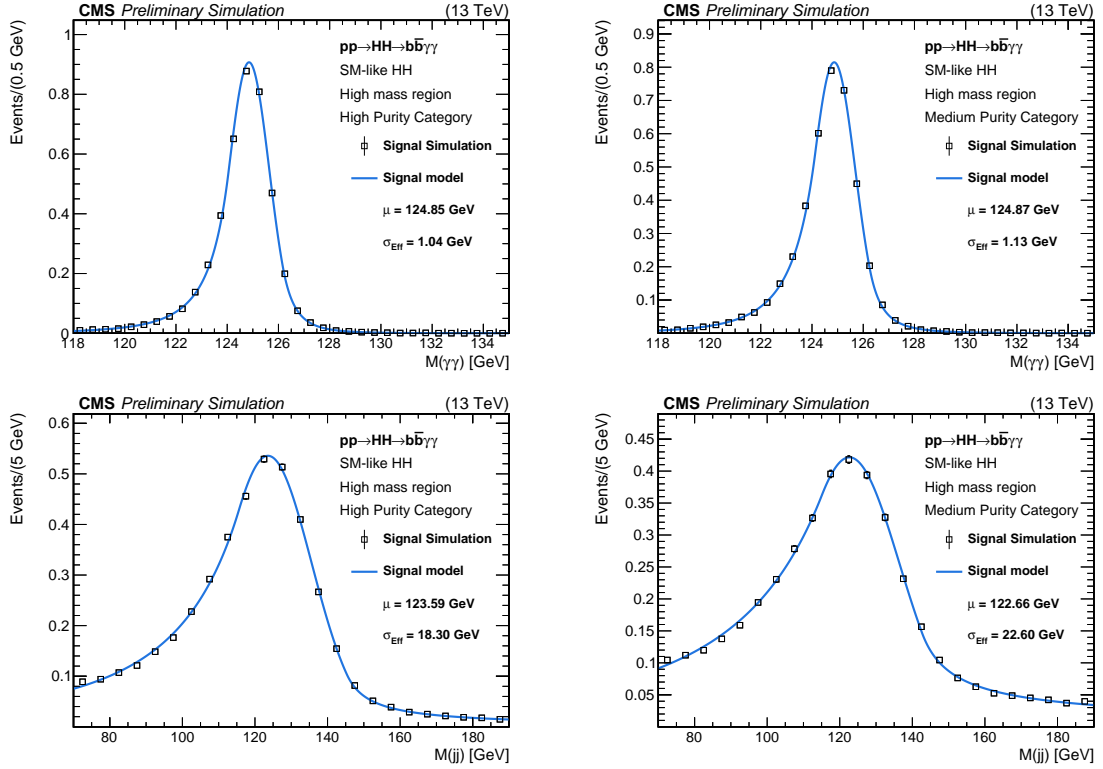
Figure 6: Signal fits for the SM HH non-resonant sample after full analysis selection, in the high mass region. The plots on the left (right) show the distributions on the HPC (MPC).
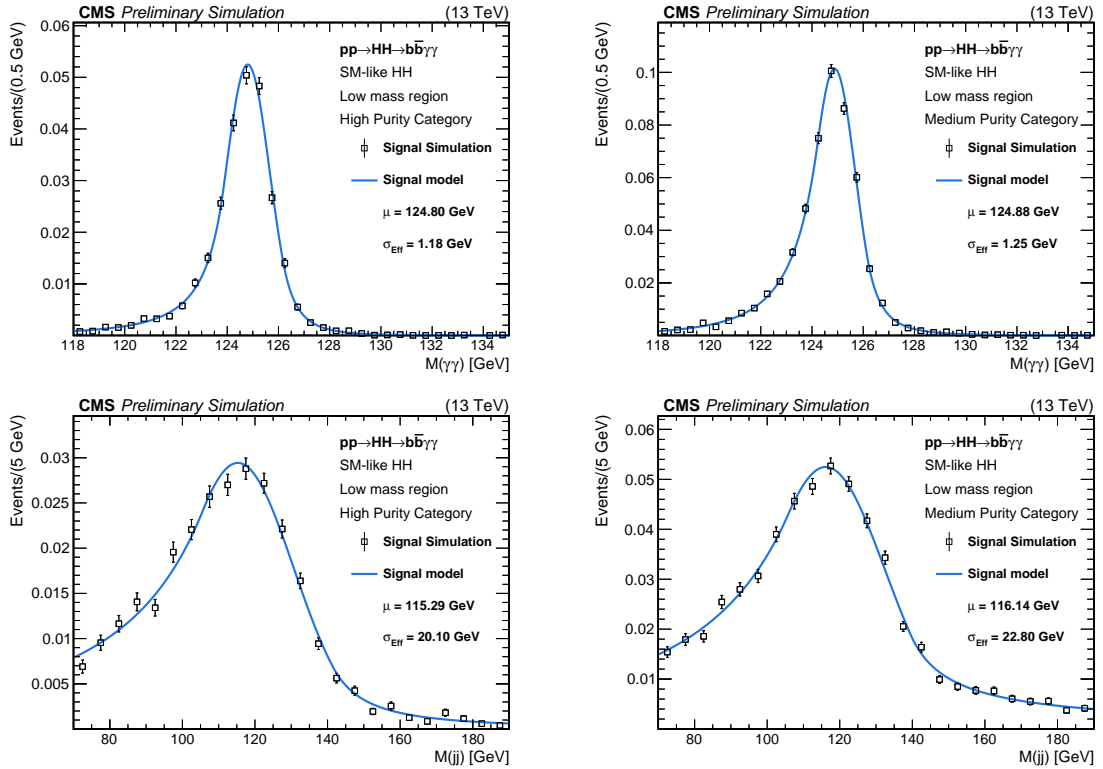

Figure 7: Signal fits for the SM HH non-resonant sample after full analysis selection, in the low mass region. The plots on the left (right) show the distributions on the HPC (MPC).
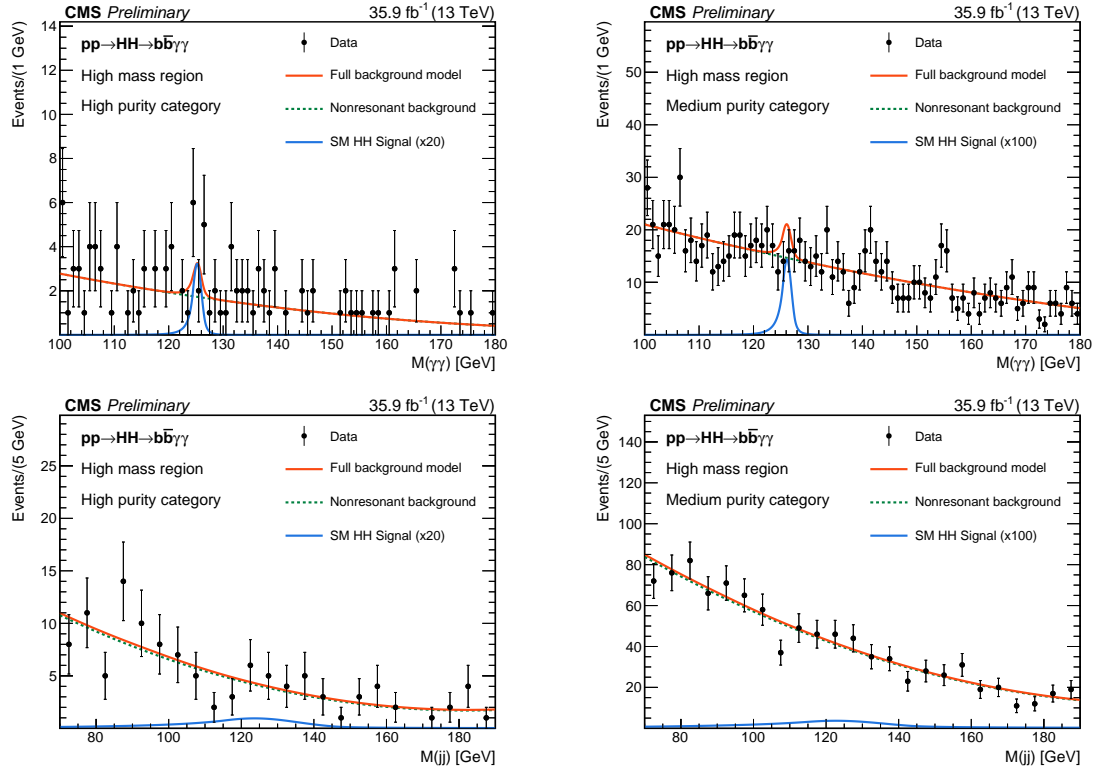
Figure 8: Background fits for the SM HH nonresonant analysis selection, in the high mass region. The plots on the left (right) show the distributions on the HPC (MPC).
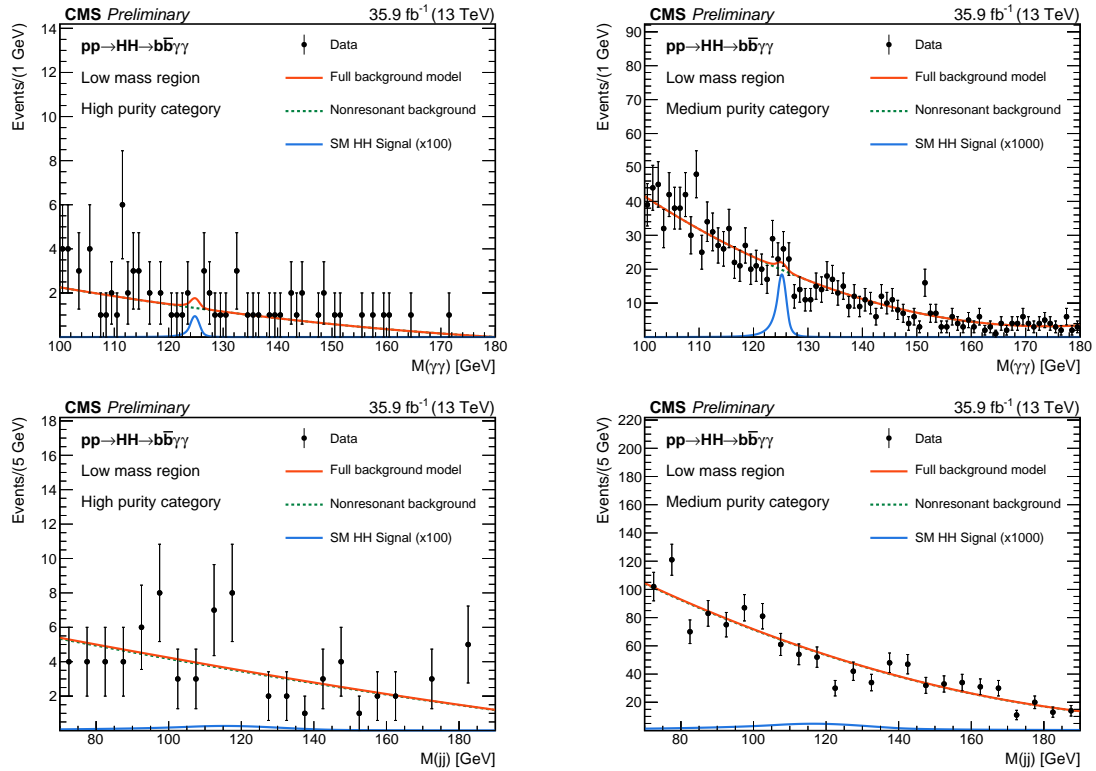

Figure 9: Background fits for the SM HH nonresonant analysis selection, in the low mass region. The plots on the left (right) show the distributions on the HPC (MPC).
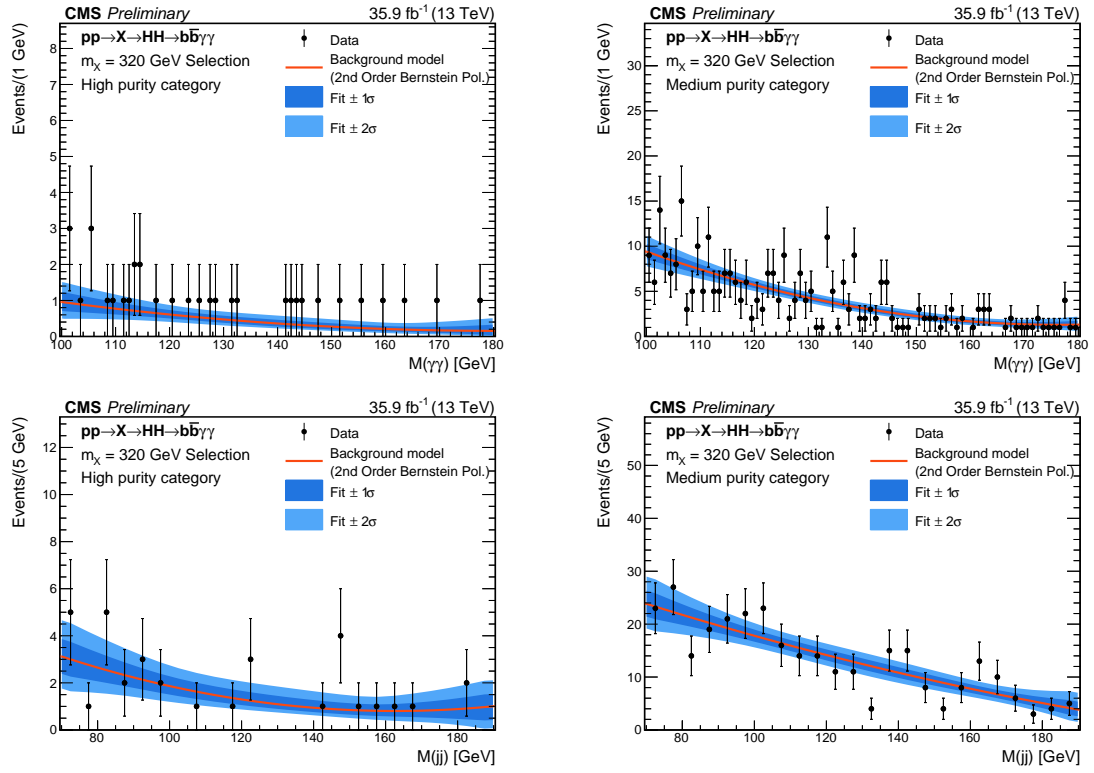
Figure 10: Background fits for the resonant analysis selection, assuming a resonance with $m_X = 320$ GeV. The plots on the left (right) show the distributions on the HPC (MPC).

6 Systematic uncertainties

The analysis defines a likelihood function based on the total PD (resonant and SM single Higgs background components and signal) and the data. The parameters for total signal and for the background-only PD are constrained in the fit to maximize this function. A uniform prior is used to parametrize the background PD. When converting the fitted yields into production cross sections, we use simulations to estimate the selection efficiency for the signal. The difference between the simulation and the data is taken into account through parameters included in the likelihood function. Parameters not of immediate interest (nuisance parameters) are varied in the fit according to a log-normal probability density function. They can be classified into two categories. The first category contains systematic uncertainties that modify the efficiency of signal selection. In particular it includes the uncertainty in the estimation of the integrated luminosity that is taken as 2.5% [56]. The second category contains the uncertainties that impact the signal or the Higgs boson PD. Included, in particular, are the $M(\gamma\gamma)$ and $M(jj)$ resolution parameters.

The photon-related uncertainties are discussed in Ref. [55]. While the photon energy scale (PES) is known at the sub-percent level in the region of p_T^γ characteristic of the SM H $\rightarrow \gamma\gamma$ signal, the uncertainty increases to 1% for $p_T^\gamma > 100$ GeV. The photon energy resolution (PER) is known with a 1% precision [55]. A 2% normalization uncertainty is estimated in the offline diphoton selection efficiency and in the trigger efficiency.

The uncertainty in the jet energy scale (JES) is accounted for by changing the jet response by 1%, while the uncertainty in the jet energy resolution (JER) is estimated by changing the jet resolution by 5%. To use the b-tagging score as an input to the classification MVA, its MC distribution is matched to data by applying differential scale factors that depend on individual jets p_T, η and their b-tagging score. The categorization MVA efficiency uncertainty is estimated by varying the b-tagging differential scale factors within one standard deviation of its uncertainties. The impact of PES, PER, JES and JER on the MVA classification procedure has been found to be negligible.

The experimental systematic uncertainties are summarized in Table 3. The uncertainty in classification MVA efficiency is anticorrelated between the high purity and medium purity categories. The same applies for the $\tilde{M}_X$ categorization, in which a normalization uncertainty is assumed and is anticorrelated in the high mass and low mass categories. In addition to the uncertainty sources listed in Table 3, theoretical uncertainties have been applied to the normalization of the SM single Higgs background, as recommended by Ref. [22].

7 Results

Upper limits on the production cross section of a pair of Higgs bosons times the branching fraction $\mathcal{B}(\text{HH} \rightarrow \text{b}\bar{\text{b}}\gamma\gamma)$ are computed using the modified frequentist approach for confidence levels (CL_s), taking the profile likelihood as a test statistics [57, 58] in the asymptotic approximation. The limits are subsequently compared to theoretical predictions assuming SM branching fractions for Higgs boson decays.

7.1 Resonant signal

The observed and median expected upper limits at 95% CL are shown in Fig. 11, for the spin-0 signal hypothesis on the left and the spin-2 hypothesis on the right. The analyzed data exclude a product of the resonances production cross sections times their branching fractions to HH $\rightarrow$ b$\bar{\text{b}}\gamma\gamma$ from 3.67 to 0.26 fb (spin-0) and from 3.61 to 0.21 fb (spin-2). The result are

Sources of Systematical Uncertainties	Type	Value
General uncertainties		
Integrated luminosity	Normalization	2.5%
Photon related uncertainties		
Photon energy scale ($\frac{\Delta M(\gamma\gamma)}{M(\gamma\gamma)}$)	Shape	1.0%
Photon energy resolution ($\frac{\Delta\sigma_{\gamma\gamma}}{\sigma_{\gamma\gamma}}$)	Shape	1.0%
Diphoton selection (with trigger uncertainties and PES)	Normalization	2.0%
Photon Identification	Normalization	1.0%
Jet related uncertainties		
Jet energy scale ($\frac{\Delta M(jj)}{M(jj)}$)	Shape	1.0%
Jet energy resolution ($\frac{\Delta\sigma_{jj}}{\sigma_{jj}}$)	Shape	5.0%
Dijet selection (JES)	Normalization	0.5%
Resonant specific uncertainties		
Mass window selection	Normalization	3.0%
Classification MVA (high purity)	Normalization	2.5%
Classification MVA (medium purity)	Normalization	1.5%
Nonresonant specific uncertainties		
$\tilde{M}_X$ Classification	Normalization	0.5%
Classification MVA (high purity)	Normalization	5%
Classification MVA (medium purity)	Normalization	2.0%

Table 3: Summary of systematic uncertainties.

compared with the cross sections for bulk radion (spin-0) and bulk KK-graviton production in WED models. The tools used to calculate the cross sections for the production of KK graviton in the bulk model are described in Refs. [59–61]. In analogy with the Higgs boson, the bulk radion field is predominantly produced through gluon-gluon fusion [62, 63]. The cross section for radion production is calculated at NLO electroweak and next-to-next-to-leading logarithmic QCD accuracy, using the recipe suggested in Ref. [64]. The observed limits are able to exclude radion resonances, assuming $\Lambda_R = 1$ TeV, for all points in the analysis mass range, and, assuming $\Lambda_R = 3$ TeV, for all mass points below $m_X = 550$ GeV. Gravitons are excluded, assuming $\kappa/M_{Pl} = 1.0$, for the mass points above $m_X = 280$ GeV and below 900 GeV, while, assuming $\kappa/M_{Pl} = 0.5$, the exclusion region is above $m_X = 300$ and below $m_X = 550$ GeV.

7.2   Nonresonant signal

The observed and expected upper limits on SM-like $pp \rightarrow HH \rightarrow b\bar{b}\gamma\gamma$ production are, respectively, 1.67 and 1.44 fb. This can be translated into 0.64 and 0.55 pb, respectively, for the total $gg \rightarrow HH$ production cross section. The results can also be interpreted in terms of observed and expected limits on the scaling factor $\mu_{HH} < 19.2$ and < 16.5, respectively. This result provides a quantification of the current analysis sensitivity relative to the SM prediction. The breakdown of this result in the different categories used for the final limit can be seen in Figure 12, in the four distinct analysis categories (LM-MPC, LM-HPC, HM-MPC and HM-HPC), in the mass regions combinations (LM and HM), and in the full combination (Combined). This figure shows that the analysis sensitivity to the SM-like HH production comes from the high mass category, which is due to the the SM $\tilde{M}_X$ distribution that peaks around 400 GeV. However, the low mass categories are important because anomalous couplings can induce the signal $\tilde{M}_X$ to peak at lower masses.

The results are also interpreted in the context of Higgs boson anomalous couplings. In Fig. 13
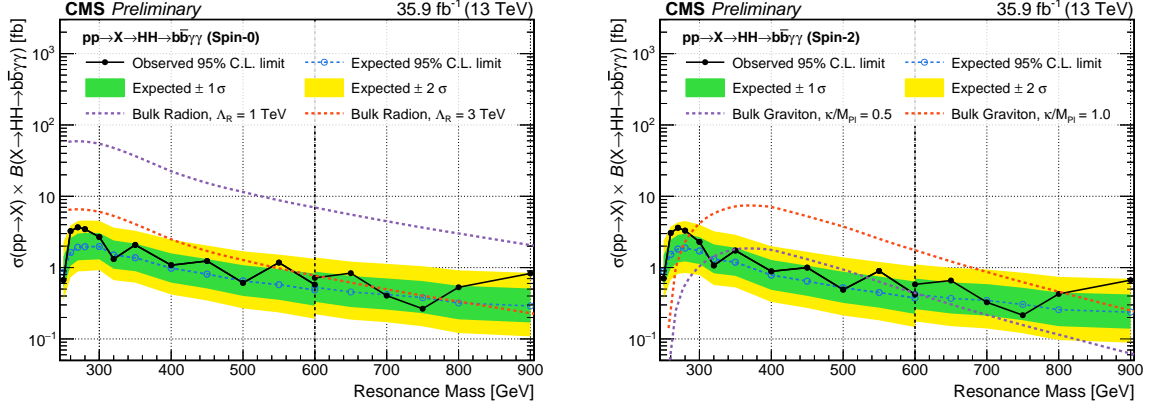
Figure 11: Observed and expected 95% C.L. upper limits on the product of cross section and the branching fraction $\sigma(pp \to X) \times \mathcal{B}(X \to HH \to b\bar{b}\gamma\gamma)$ obtained through a combination of the two event categories. The green and yellow bands represent, respectively, the 1 and 2 standard deviation extensions beyond the expected limit. Also shown are theoretical predictions corresponding to WED models for bulk radions (left) and bulk KK-gravitons (right). The vertical dashed line in the upper plot shows the separation between the low mass and high mass regions. The limits for $m_X = 600$ GeV are shown for both methods.
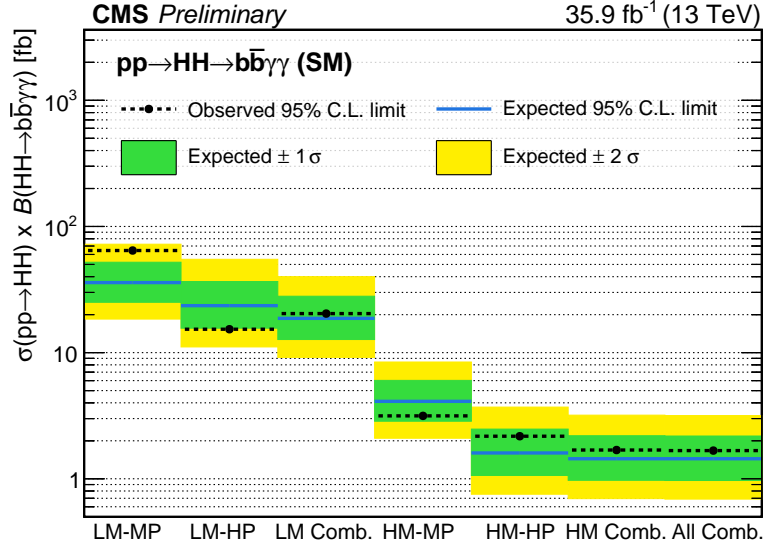

Figure 12: Expected 95% C.L. upper limits on the product of cross section and the branching fraction $\sigma(pp \to HH \times \mathcal{B}(HH \to b\bar{b}\gamma\gamma)$ obtained through a combination of different event categories. The green and yellow bands represent, respectively, the 1 and 2 standard deviation extensions beyond the expected limit.

(left), 95% CL limits on the nonresonant Higgs pair production cross sections are shown, assuming coupling changes that maintain the ratio κ_λ/κ_t fixed while the other parameters are fixed to their SM values. Assuming that the top quark Yukawa coupling is SM-like ($\kappa_t = 1$), the analysis observes limits that constrain κ_λ between -8.82 and 15.04. In Fig. 13 (right), a scan in 2D in κ_t and κ_λ is performed while fixing the other parameters to their SM values.
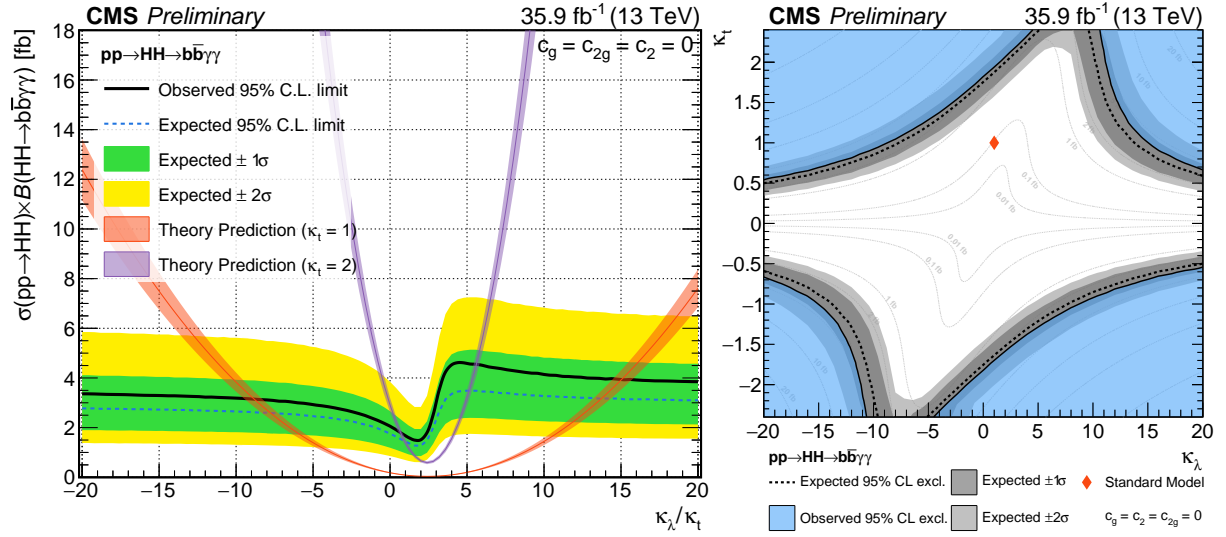
Figure 13: On the left, upper limits for the BSM models with varying κ_λ parameter, while the others are fixed to their SM values. On the right, exclusion regions for models with varying κ_λ and κ_t parameters, while the others are fixed to their SM values.

8 Conclusion

A search is performed by the CMS collaboration for resonant and nonresonant production of two Higgs bosons in the decay channel $HH \rightarrow b\bar{b}\gamma\gamma$, based on an integrated luminosity of $35.9\,\text{fb}^{-1}$ of pp collisions collected at $\sqrt{s} = 13\,\text{TeV}$ in 2016. Resonances are investigated in the mass range between 250 and 900 GeV, under spin-0 and spin-2 hypotheses. Expected and observed upper limits at a 95% CL are measured on the cross sections for the production of new particles decaying to $HH \rightarrow b\bar{b}\gamma\gamma$. The limits are compared to BSM predictions, based on the assumption of the existence of a warped extra dimension. No statistically significant deviations from the null hypothesis are found. The observed limits exclude the radion (spin-0) signal hypothesis, assuming $\Lambda_R = 3$ TeV, for all mass points below $m_X = 550$ GeV, and exclude the graviton (spin-2) hypothesis, assuming $\kappa/M_{Pl} = 1.0$, for the mass points above $m_X = 280$ GeV and below 900 GeV. For nonresonant production with SM-like kinematics, a 95% CL upper limit is set on $\sigma(pp \rightarrow HH) \times \mathcal{B}(HH \rightarrow b\bar{b}\gamma\gamma)$ at 1.67 fb. Anomalous couplings of the Higgs boson are also investigated. Exclusions are performed on the effective Higgs boson self coupling (κ_λ) for $\kappa_\lambda > -8.82$ and $\kappa_\lambda < 15.04$, assuming all other Higgs couplings to be SM-like. Additionally, exclusions are performed on the two-dimensional plane in which both κ_λ and the Higgs-top quark Yukawa coupling vary.

References

[1] CMS Collaboration, "Observation of a new boson at a mass of 125 GeV with the CMS experiment at the LHC", *Phys.Lett.* **B716** (2012), no. CMS-HIG-12-028, CERN-PH-EP-2012-220, 30–61, `doi:10.1016/j.physletb.2012.08.021`, `arXiv:1207.7235`.

[2] ATLAS Collaboration, "Observation of a new particle in the search for the standard model Higgs boson with the ATLAS detector at the LHC", *Phys.Lett.* **B716** (2012), no. CERN-PH-EP-2012-218, 1–29, `doi:10.1016/j.physletb.2012.08.020`, `arXiv:1207.7214`.

[3] D. de Florian and J. Mazzitelli, "Higgs Boson Pair Production at Next-to-Next-to-Leading Order in QCD", *Phys. Rev. Lett.* **111** (2013) 201801, `doi:10.1103/PhysRevLett.111.201801, arXiv:1309.6594`.

[4] J. Baglio et al., "The measurement of the Higgs self-coupling at the LHC: theoretical status", *JHEP* **04** (2013) 151, `doi:10.1007/JHEP04(2013)151, arXiv:1212.5581`.

[5] S. Dawson, A. Ismail, and I. Low, "What is in the loop? The anatomy of double Higgs production", *Phys. Rev.* **D91** (2015), no. 11, 115008, `doi:10.1103/PhysRevD.91.115008, arXiv:1504.05596`.

[6] Z. Heng, L. Shang, Y. Zhang, and J. Zhu, "Pair production of 125 GeV Higgs boson in the SM extension with color-octet scalars at the LHC", *JHEP* **02** (2014) 083, `doi:10.1007/JHEP02(2014)083, arXiv:1312.4260`.

[7] L. Randall and R. Sundrum, "A Large mass hierarchy from a small extra dimension", *Phys.Rev.Lett.* **83** (1999), no. MIT-CTP-2860, PUPT-1860, BUHEP-99-9, 3370–3373, `doi:10.1103/PhysRevLett.83.3370, arXiv:hep-ph/9905221`.

[8] W. D. Goldberger and M. B. Wise, "Modulus stabilization with bulk fields", *Phys.Rev.Lett.* **83** (1999), no. CALT-68-2232, 4922–4925, `doi:10.1103/PhysRevLett.83.4922, arXiv:hep-ph/9907447`.

[9] O. DeWolfe, D. Freedman, S. Gubser, and A. Karch, "Modeling the fifth-dimension with scalars and gravity", *Phys.Rev.* **D62** (2000), no. HUTP-99-A048, MIT-CTP-2903, 046008, `doi:10.1103/PhysRevD.62.046008, arXiv:hep-th/9909134`.

[10] C. Csaki, M. Graesser, L. Randall, and J. Terning, "Cosmology of brane models with radion stabilization", *Phys.Rev.* **D62** (2000), no. SCIPP-99-49, HUTP-A061, NSF-ITP-99-130, 045015, `doi:10.1103/PhysRevD.62.045015, arXiv:hep-ph/9911406`.

[11] H. Davoudiasl, J. L. Hewett, and T. G. Rizzo, "Phenomenology of the Randall-Sundrum Gauge Hierarchy Model", *Phys. Rev. Lett.* **84** (2000), no. SLAC-PUB-8241, 2080, `doi:10.1103/PhysRevLett.84.2080, arXiv:hep-ph/9909255`.

[12] C. Csaki, M. L. Graesser, and G. D. Kribs, "Radion dynamics and electroweak physics", *Phys.Rev.* **D63** (2001), no. SCIPP-00-27, 065002, `doi:10.1103/PhysRevD.63.065002, arXiv:hep-th/0008151`.

[13] K. Agashe, H. Davoudiasl, G. Perez, and A. Soni, "Warped Gravitons at the LHC and Beyond", *Phys.Rev.* **D76** (2007), no. SU-4252-843, BNL-HET-07-3, YITP-SB-07-02, 036006, `doi:10.1103/PhysRevD.76.036006, arXiv:hep-ph/0701186`.

[14] A. L. Fitzpatrick, J. Kaplan, L. Randall, and L.-T. Wang, "Searching for the Kaluza-Klein Graviton in Bulk RS Models", *JHEP* **0709** (2007) 013, `doi:10.1088/1126-6708/2007/09/013, arXiv:hep-ph/0701150`.

[15] G. C. Branco et al., "Theory and phenomenology of two-Higgs-doublet models", *Phys. Rept.* **516** (2012) 1–102, `doi:10.1016/j.physrep.2012.02.002, arXiv:1106.0034`.

[16] A. Djouadi et al., "Fully covering the MSSM Higgs sector at the LHC", *JHEP* **06** (2015) 168, `doi:10.1007/JHEP06(2015)168, arXiv:1502.05653`.

[17] R. Grober and M. Muhlleitner, "Composite Higgs Boson Pair Production at the LHC", *JHEP* **06** (2011), no. KA-TP-37-2010, 020, `doi:10.1007/JHEP06(2011)020`, `arXiv:1012.1562`.

[18] M. Moretti et al., "Higgs boson self-couplings at the LHC as a probe of extended Higgs sectors", *JHEP* **02** (2005), no. FNT-T-2004-03, SHEP-03-12, CAFPE-26-03, UG-FT-156-03, LAPTH-1028-04, BA-TH-495-04, 024, `doi:10.1088/1126-6708/2005/02/024`, `arXiv:hep-ph/0410334`.

[19] A. Pierce, J. Thaler, and L.-T. Wang, "Disentangling dimension six operators through di-Higgs boson production", *JHEP* **05** (2007) 070, `doi:10.1088/1126-6708/2007/05/070`, `arXiv:hep-ph/0609049`.

[20] A. Carvalho Antunes De Oliveira et al., "Analytical parametrization and shape classification of anomalous HH production in EFT approach", Technical Report LHCHXSWG-2016-001, CERN, Geneva, Jul, 2016.

[21] J. Grigo, K. Melnikov, and M. Steinhauser, "Virtual corrections to Higgs boson pair production in the large top quark mass limit", *Nucl. Phys.* **B888** (2014) 17–29, `doi:10.1016/j.nuclphysb.2014.09.003`, `arXiv:1408.2422`.

[22] LHC Higgs Cross Section Working Group Collaboration, "Handbook of LHC Higgs Cross Sections: 4. Deciphering the Nature of the Higgs Sector", `doi:10.23731/CYRM-2017-002`, `arXiv:1610.07922`.

[23] G. F. Giudice, C. Grojean, A. Pomarol, and R. Rattazzi, "The Strongly-Interacting Light Higgs", *JHEP* **06** (2007) 045, `doi:10.1088/1126-6708/2007/06/045`, `arXiv:hep-ph/0703164`.

[24] S. Heinemeyer et al., "Handbook of LHC Higgs cross sections: 3. Higgs properties", CERN Report CERN-2013-004, 2013. `doi:10.5170/CERN-2013-004`, `arXiv:1307.1347`.

[25] CMS Collaboration, "Search for two Higgs bosons in final states containing two photons and two bottom quarks in proton-proton collisions at 8 TeV", *Phys. Rev.* **D94** (2016), no. 5, 052012, `doi:10.1103/PhysRevD.94.052012`, `arXiv:1603.06896`.

[26] ATLAS Collaboration, "Search For Higgs Boson Pair Production in the $\gamma\gamma b\bar{b}$ Final State using pp Collision Data at $\sqrt{s} = 8$ TeV from the ATLAS Detector", *Phys. Rev. Lett.* **114** (2015), no. CERN-PH-EP-2014-113, 081802, `doi:10.1103/PhysRevLett.114.081802`, `arXiv:1406.5053`.

[27] ATLAS Collaboration, "Search for Higgs boson pair production in the $b\bar{b}b\bar{b}$ final state from pp collisions at $\sqrt{s} = 8$ TeV with the ATLAS detector", *Eur. Phys. J. C* **75** (2015), no. CERN-PH-EP-2015-099, 412, `doi:10.1140/epjc/s10052-015-3628-x`, `arXiv:1506.00285`.

[28] ATLAS Collaboration, "Searches for Higgs boson pair production in the $hh \rightarrow bb\tau\tau, \gamma\gamma WW^*, \gamma\gamma bb, bbbb$ channels with the ATLAS detector", *Phys. Rev. D* **92** (2015), no. CERN-PH-EP-2015-225, 092004, `doi:10.1103/PhysRevD.92.092004`, `arXiv:1509.04670`.

[29] CMS Collaboration, "Searches for heavy Higgs bosons in two-Higgs-doublet models and for t → ch decay using multilepton and diphoton final states in pp collisions at 8 TeV", *Phys. Rev. D* **90** (2014) 112013, `doi:10.1103/PhysRevD.90.112013`, `arXiv:1410.2751`.

[30] CMS Collaboration, "Search for resonant pair production of Higgs bosons decaying to two bottom quark-antiquark pairs in proton-proton collisions at 8 TeV", *Phys. Lett. B* **749** (2015) 560, `doi:10.1016/j.physletb.2015.08.047`, `arXiv:1503.04114`.

[31] CMS Collaboration, "Search for heavy resonances decaying to two Higgs bosons in final states containing four b quarks", *Eur. Phys. J. C* **76** (2016) 371, `doi:10.1140/epjc/s10052-016-4206-6`, `arXiv:1602.08762`.

[32] CMS Collaboration, "Searches for a heavy scalar boson H decaying to a pair of 125 GeV Higgs bosons hh or for a heavy pseudoscalar boson A decaying to Zh, in the final states with h → ττ", *Phys. Lett. B* **755** (2016) 217, `doi:10.1016/j.physletb.2016.01.056`, `arXiv:1510.01181`.

[33] CMS Collaboration, "The CMS experiment at the CERN LHC", *JINST* **3** (2008) S08004, `doi:10.1088/1748-0221/3/08/S08004`.

[34] J. Alwall et al., "The automated computation of tree-level and next-to-leading order differential cross sections, and their matching to parton shower simulations", *JHEP* **07** (2014) 079, `doi:10.1007/JHEP07(2014)079`, `arXiv:1405.0301`.

[35] A. Buckley et al., "LHAPDF6: parton density access in the LHC precision era", *Eur. Phys. J.* **C75** (2015), no. GLAS-PPE-2014-05, MCNET-14-29, IPPP-14-111, DCPT-14-222, 132, `doi:10.1140/epjc/s10052-015-3318-8`, `arXiv:1412.7420`.

[36] J. Butterworth et al., "PDF4LHC recommendations for LHC Run II", `arXiv:1510.03865`.

[37] T. Sjostrand, S. Mrenna, and P. Z. Skands, "A Brief Introduction to PYTHIA 8.1", *Comput. Phys. Commun.* **178** (2008), no. CERN-LCGAPP-2007-04, LU-TP-07-28, FERMILAB-PUB-07-512-CD-T, 852–867, `doi:10.1016/j.cpc.2008.01.036`, `arXiv:0710.3820`.

[38] GEANT4 Collaboration, "GEANT4 – a simulation toolkit", *Nucl. Instrum. Meth. A* **506** (2003), no. SLAC-PUB-9350, FERMILAB-PUB-03-339, 250, `doi:10.1016/S0168-9002(03)01368-8`.

[39] ATLAS and CMS Collaborations, "Combined Measurement of the Higgs Boson Mass in pp Collisions at $\sqrt{s} = 7$ and 8 TeV with the ATLAS and CMS Experiments", *Phys. Rev. Lett.* **114** (2015) 191803, `doi:10.1103/PhysRevLett.114.191803`, `arXiv:1503.07589`.

[40] A. Carvalho et al., "Higgs Pair Production: Choosing Benchmarks With Cluster Analysis", *JHEP* **04** (2016) 126, `doi:10.1007/JHEP04(2016)126`, `arXiv:1507.02245`.

[41] A. Carvalho et al., "Analytical parametrization and shape classification of anomalous HH production in the EFT approach", `arXiv:1608.06578`.

[42] B. Mellado Garcia, P. Musella, M. Grazzini, and R. Harlander, "CERN Report 4: Part I Standard Model Predictions", Technical Report LHCHXSWG-DRAFT-INT-2016-008, May, 2016.

[43] P. Nason, "A new method for combining NLO QCD with shower Monte Carlo algorithms", *JHEP* **11** (2004) 040, `doi:10.1088/1126-6708/2004/11/040`, `arXiv:hep-ph/0409146`.

[44] S. Frixione, P. Nason, and C. Oleari, "Matching NLO QCD computations with Parton Shower simulations: the POWHEG method", *JHEP* **11** (2007), no. BICOCCA-FT-07-9, GEF-TH-21-2007, 070, `doi:10.1088/1126-6708/2007/11/070`, `arXiv:0709.2092`.

[45] S. Alioli, P. Nason, C. Oleari, and E. Re, "A general framework for implementing NLO calculations in shower Monte Carlo programs: the POWHEG BOX", *JHEP* **06** (2010) 043, `doi:10.1007/JHEP06(2010)043`, `arXiv:1002.2581`.

[46] CMS Collaboration, "Measurements of properties of the Higgs boson in the diphoton decay channel with the full 2016 data set", CMS Physics Analysis Summary CMS-PAS-HIG-16-040, CERN, Geneva, 2017.

[47] CMS Collaboration, "Electron and photon performance in CMS with the full 2016 data sample.", CMS Detector Performance Note CMS-DP-2017-004, 2017.

[48] CMS Collaboration, "Particle-flow reconstruction and global event description with the CMS detector", (2017). `arXiv:1706.04965`. Submitted to *JINST*.

[49] CMS Collaboration, "Identification of b quark jets at the CMS Experiment in the LHC Run 2", CMS Physics Analysis Summary CMS-PAS-BTV-15-001, CERN, Geneva, 2016.

[50] CMS Collaboration, "Search for the standard model Higgs boson produced through vector boson fusion and decaying to bb with proton-proton collisions at sqrt(s) = 13 TeV", CMS Physics Analysis Summary CMS-PAS-HIG-16-003, 2016.

[51] N. Kumar and S. P. Martin, "LHC search for di-Higgs decays of stoponium and other scalars in events with two photons and two bottom jets", *Phys. Rev.* **D90** (2014), no. 5, 055007, `doi:10.1103/PhysRevD.90.055007`, `arXiv:1404.0996`.

[52] S. Bolognesi et al., "On the spin and parity of a single-produced resonance at the LHC", *Phys. Rev.* **D86** (2012) 095031, `doi:10.1103/PhysRevD.86.095031`, `arXiv:1208.4018`.

[53] A. Hoecker et al., "TMVA: Toolkit for Multivariate Data Analysis", *PoS* **ACAT** (2007) 040, `arXiv:physics/0703039`.

[54] M. J. Oreglia, "A study of the reactions $\psi' \to \gamma\gamma\psi$". PhD thesis, Stanford University, 1980. SLAC Report SLAC-R-236.

[55] CMS Collaboration, "Observation of the diphoton decay of the Higgs boson and measurement of its properties", *Eur. Phys. J. C* **74** (2014) 3076, `doi:10.1140/epjc/s10052-014-3076-z`, `arXiv:1407.0558`.

[56] CMS Collaboration, "CMS Luminosity Measurements for the 2016 Data Taking Period", CMS Physics Analysis Summary CMS-PAS-LUM-17-001, CERN, Geneva, 2017.

[57] A. L. Read, "Presentation of search results: the CL$_s$ technique", *J. Phys. G* **28** (2002) 2693, `doi:10.1088/0954-3899/28/10/313`.

[58] T. Junk, "Confidence level computation for combining searches with small statistics", *Nucl. Instrum. Meth. A* **434** (1999) 435, `doi:10.1016/S0168-9002(99)00498-2`, `arXiv:hep-ex/9902006`.

[59] K. Agashe et al., "Warped Extra Dimensional Benchmarks for Snowmass 2013", in *Community Summer Study 2013: Snowmass on the Mississippi (CSS2013) Minneapolis, MN, USA, July 29-August 6, 2013.* 2013. `arXiv:1309.7847`.

[60] P. de Aquino, K. Hagiwara, Q. Li, and F. Maltoni, "Simulating graviton production at hadron colliders", *JHEP* **06** (2011) 132, `doi:10.1007/JHEP06(2011)132`, `arXiv:1101.5499`.

[61] A. Oliveira, "Gravity particles from Warped Extra Dimensions, a review. Part I - KK Graviton", (2014). `arXiv:1404.0102`.

[62] U. Mahanta and A. Datta, "Search prospects of light stabilized radions at Tevatron and LHC", *Phys. Lett. B* **483** (2000) 196, `doi:10.1016/S0370-2693(00)00560-8`, `arXiv:hep-ph/0002183`.

[63] H. Davoudiasl, J. Hewett, and T. Rizzo, "Experimental probes of localized gravity: On and off the wall", *Phys.Rev.* **D63** (2001), no. SLAC-PUB-8436, 075004, `doi:10.1103/PhysRevD.63.075004`, `arXiv:hep-ph/0006041`.

[64] G. F. Giudice, R. Rattazzi, and J. D. Wells, "Graviscalars from higher dimensional metrics and curvature Higgs mixing", *Nucl.Phys.* **B595** (2001), no. CERN-TH-2000-051, SNS-PH-2000-03, UCD-2000-7, LBNL-45201, LBL-45201, 250–276, `doi:10.1016/S0550-3213(00)00686-6`, `arXiv:hep-ph/0002178`.